ADVANCED FUNCTIONAL MATERIALS

DOI: 10.1002/adfm.200700653

One-Step Solvent-Free Synthesis and Characterization of $Zn_{1-x}Mn_xSe$@C Nanorods and Nanowires**

By *Sayan Bhattacharyya, Ilana Perelshtein, Ofer Moshe, Daniel H. Rich,* and *Aharon Gedanken**

The carbon-encapsulated, Mn-doped ZnSe ($Zn_{1-x}Mn_xSe$@C) nanowires, nanorods, and nanoparticles are synthesized by the solvent-free, one-step RAPET (reactions under autogenic pressure at elevated temperature) approach. The aspect ratio of the nanowires/nanorods is altered according to the Mn/Zn atomic ratio, with the maximum being observed for Mn/Zn = 1:20. A 10–20 nm amorphous carbon shell is evidenced from electron microscopy analysis. The replacement of Zn by Mn in the $Zn_{1-x}Mn_xSe$ lattice is confirmed by the hyperfine splitting values in the electron paramagnetic resonance (EPR) experiments. Raman experiments reveal that the $Zn_{1-x}Mn_xSe$ core is highly crystalline, while the shell consists of disordered graphitic carbon. Variable-temperature cathodoluminescence measurements are performed for all samples and show distinct ZnSe near-band-edge and Mn-related emissions. An intense and broad Mn-related emission at the largest Mn alloy composition of 19.9% is further consistent with an efficient incorporation of Mn within the host ZnSe lattice. The formation of the core/shell nanowires and nanorods in the absence of any template or structure-directing agent is controlled kinetically by the $Zn_{1-x}Mn_xSe$ nucleus formation and subsequent carbon encapsulation. Mn replaces Zn mainly in the (111) plane and catalyzes the nanowire growth in the [111] direction.

1. Introduction

Zinc selenide is a wide bandgap II–VI semiconductor material ($E_g = 2.8$ eV) and has a wide range of applications in optoelectronic devices.[1] In nanometer dimensions, zinc selenides (ZnSe) have been reported as one-dimensional (1D) nanostructures such as nanowires and nanorods,[1a,2] spherical nanoparticles,[3] and also as micrometer-sized spheres and tubes.[4] The high success and potential of the pure nanometer-scale ZnSe semiconductor crystallites have encouraged researchers worldwide to dope (intentional introduction of impurities) the nanocrystals with transition-metal ions.[5] The Mn^{2+} ion is an efficient dopant, since Mn^{2+} acts as a paramagnetic center (electron spin, $S = 5/2$), replacing the Zn^{2+} in the ZnSe lattice.[5a] The sp–d exchange interaction occurs between ZnSe and Mn as a result of the spin–spin exchange interactions, which give rise to interesting magnetic and magneto-optical properties.[5a] These materials represent a particular class of diluted magnetic semiconductors (DMS) in the field of spintronics.[6] According to thermodynamics, Mn^{2+} ions can be incorporated into II–VI semiconductors up to their solid solubility limit (ca. 50%).[5b] However, the synthesis of efficiently Mn^{2+}-doped semiconductors is always difficult, since Mn has a tendency to be expelled to the ZnSe nanocrystal surface by a 'self-purification' mechanism.[5a,b] Hence, it is a challenge to synthesize high-quality Mn-doped ZnSe with the Mn actually embedded inside the ZnSe unit cell. Moreover, all the ZnSe nanocrystals successfully doped with individual Mn atoms exhibit a zinc blende crystal structure.[5b] The methods that have been used to synthesize Mn-doped ZnSe nanostructures include thermal evaporation,[7] molecular-beam epitaxy,[8] and chemical synthesis involving organic solvents.[5,9] To the best of our knowledge, until now there has only been one report on $Zn_{1-x}Mn_xSe$ 1D nanostructures,[7] and another report on the general method of II–VI DMS nanowires.[10] 1D nanostructures, such as nanowires, nanobelts, nanotubes, and nanorods, are very much sought-after materials for the fabrication of novel nanoscale devices.[11]

Semiconductor quantum dots (QDs) represent one of the bridging interfaces between nanoscience/nanotechnology and biology. The importance is due to their unique optical properties.[12a] However, many of the bare II–VI semiconductor materials, such as CdSe and ZnS QDs, are highly toxic to biological tissue.[12b] CdSe/ZnS QDs were made water-soluble and biocompatible by coating them with silica.[12c] The silica-coated CdSe/ZnS semiconductor nanocrystals were also used for biological imaging.[12d] Recently, the 6.2 nm Mn^{2+}-

[*] Prof. A. Gedanken, Dr. S. Bhattacharyya, I. Perelshtein
Department of Chemistry, and
Kanbar Laboratory for Nanomaterials at the Bar-Ilan University
Center for Advanced
Materials and Nanotechnology, Bar-Ilan University
Ramat-Gan 52900 (Israel)
E-mail: gedanken@mail.biu.ac.il
O. Moshe, Prof. D. H. Rich
Department of Physics, The Ilse Katz Institute for Nanoscience and Nanotechnology
Ben-Gurion University of the Negev
P.O. Box 653, Beer-Sheva 84105 (Israel)

[**] This research work was supported by a Strategic-Infrastructure grant from the Israeli Ministry of Science, Sport and Culture.

doped ZnSe QDs were made water-soluble by coating them with a monolayer of mercaptopropionic acid to make them useful as biomedical labeling reagents.[9e] For these reasons, the carbon coating of transition-metal-doped ZnSe nanomaterials has the ability to reduce their toxicity and make them amenable for biological applications. Over the years, the coating of several materials with diamond, graphite-like, and amorphous carbon has immensely increased their biocompatibility and biomedicinal applications.[13] Moreover, during the last decade, researchers have focused on the fabrication of single-crystal metals and nanomaterials encapsulated by graphite layers because of the fascinating properties of such core/shell nanostructures.[14] Janotta et al. reported on the protection of the optical properties and chemical integrity of the diamond-like carbon-coated ZnSe waveguides,[15] and Geng et al. reported on the enhanced blue emission of carbon-encapsulated ZnSe nanoparticles.[16] The bare semiconductor nanoparticles tend to aggregate and easily oxidize. In the case of carbon-encapsulated semiconductor nanocrystals, the carbon shell offers excellent protection to the semiconductor core, which is potentially important for optoelectronic and magnetic nanodevices.

In this Full Paper, we report on the successful, solvent-free, one-step synthesis of carbon-encapsulated, manganese-doped ZnSe nanowires, nanorods, and nanoparticles via the straightforward RAPET (reactions under autogenic pressure at elevated temperature) approach. The core/shell nanowires and nanorods were formed without the use of any template or structure-directing agent. The $Zn_{1-x}Mn_xSe$@C products with Mn/Zn atomic ratios of 0, 0.01, 0.049, 0.101, and 0.199 are determined by inductively coupled plasma (ICP) analysis. This corresponds to Mn/Zn ratios of 0, 1:100, 1:20, 1:10, and 1:5 and designated as ZM0, ZM1, ZM2, ZM3 and ZM4, respectively, and will be referred to accordingly in subsequent discussions. The electron paramagnetic resonance (EPR) studies confirmed the efficient Mn doping inside the ZnSe lattice. An intense and broad Mn-related luminescence at the largest Mn alloy concentration of 19.9%, as measured with variable temperature cathodoluminescence (CL), is further consistent with the efficient incorporation of Mn within the host ZnSe crystal. Indeed, a survey of the experimental literature reveals that carbon-encapsulated, Mn-doped ZnSe 1D nanostructures have not been previously reported. Moreover, the solvent-free RAPET technique involves a 'beakerless' synthesis, which is cheap and much less cumbersome than all other previously reported methods.

2. Results and Discussion

The X-ray diffraction (XRD) patterns of the $Zn_{1-x}Mn_xSe$@C products are shown in Figure 1. All the reflection peaks in the products could be readily indexed to the cubic, zinc blende ZnSe (*F*–43*m* space group), which agrees well with the reported data (Joint Committee on Powder Diffraction Standards (JCPDS) card no. 37-1463). The (111) reflection peak is shifted when Mn substitutes the Zn sites in the $Zn_{1-x}Mn_xSe$ lattice. From ZM0 to ZM4, the shift ($\Delta 2\theta$) of the (111) reflection peak is towards lower 2θ values. Using the Vegard's rule [$a(x) = (1-x)a_{ZnSe} + xa_{MnSe}$, where, a_{ZnSe} and a_{MnSe} are the cubic lattice constants of ZnSe (0.56696 nm) and MnSe (0.59022 nm), respectively],[17] the lattice parameter *a* was calculated as 0.56719, 0.56810, 0.56931, and 0.57159 nm for ZM1, ZM2, ZM3, and ZM4, respectively. Thus *a* varies linearly with the Mn content (*x*). The ionic radii of Mn^{2+} and Zn^{2+} are 0.80 and 0.74 Å, respectively, and hence the Mn^{2+} doping causes an overall expansion of the lattice. The reaction conditions are controlled in order to remove any impurity phase (ZnO and Se) formation, and such peaks are not detected in the XRD patterns. Graphitic carbon XRD peaks are not observed as it might be in an amorphous or semicrystalline state. We could not detect the MnSe diffraction peaks because Mn^{2+} ions replaced Zn^{2+} in the ZnSe unit cell.

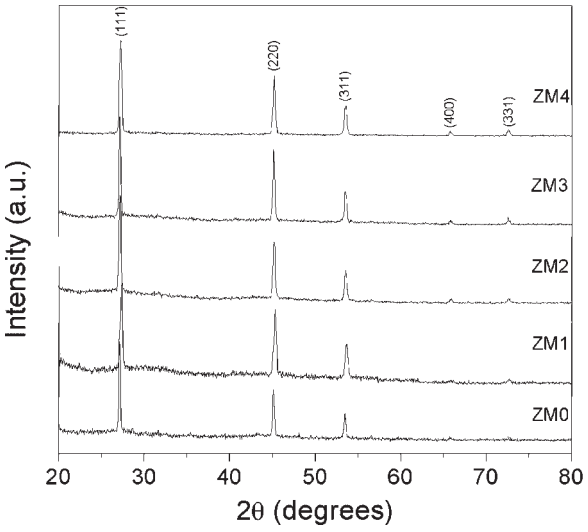

Figure 1. XRD patterns taken from the synthesized $Zn_{1-x}Mn_xSe$@C products products.

In order to investigate the relation of the shape and size of the nanostructures to the Mn/Zn atomic ratio, we measured the high- and low-resolution scanning/transmission electron microscopy (SEM/TEM) for the prepared products. The images are important and help in proposing a formation and growth mechanism. The high-resolution SEM (HRSEM) images in Figure 2 show a variety of morphologies for the products. The nanorods are observed protruding out of a common base in ZM0 (Fig. 2a). A careful observation of the image reveals a core/shell structure of the nanorods. The morphology and dimension of the nanostructures are presented in Table 1. The SEM image of ZM1 (Fig. 2b) displays a mixture of shapes such as small anisotropic particles, a bundle of elongated nanowires, and microspheres of irregular size. An enlarged view of the small anisotropic particles (Fig. 2c) shows core/shell nanorods of aspect ratio (AR) = 1.7. The micro-

ADVANCED FUNCTIONAL MATERIALS

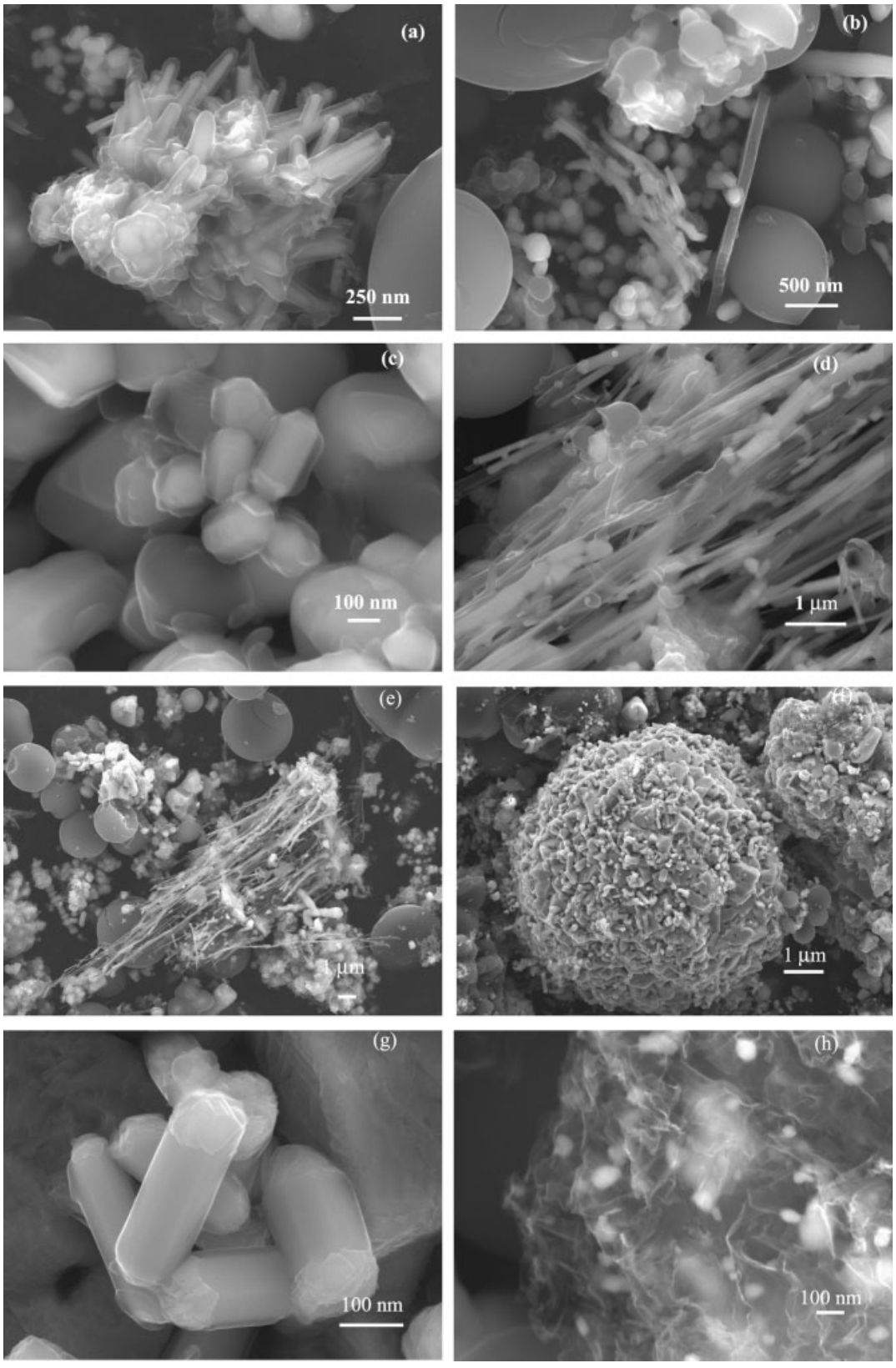

Figure 2. HRSEM images: a) ZM0, b,c) ZM1, low and high magnification, respectively, d,e) ZM2, high and low magnification, respectively, f,g) ZM3, low and high magnification, respectively, and h) ZM4.

Table 1. Morphology of the products obtained, as measured from HRSEM and TEM/HRTEM images. *D* = diameter, *L* = length, *AR* = aspect ratio, *C* = core thickness, *S* = shell thickness. All dimensions are presented in nanometers, if not otherwise stated. Values in brackets represent one standard deviation.

Name	Morphology	HRSEM					TEM/HRTEM				
		D	*L*	*AR*	*C*	*S*	*D*	*L*	*AR*	*C*	*S*
ZM0	Nanorods	97 (5)	≥430	4.5	57 (7)	20 (3)	104	475	4.5	68	14–18
ZM1	Nanorods	121 (11)	200	1.7	85 (5)	18 (2)	107 (2)	150 (14)	1.4	65 (1)	21.0 (0.4)
	Nanowires	114	2 μm	18	—	—					
ZM2	Nanowires	120 (15)	21 μm	175	—	—	90 (1)	>1.4 μm, 550	~16		
ZM3	Nanorods	111 (12)	241 (20)	2.2	—	—	116	537	4.6	94	8–16
ZM4	Spherical	55 (8)	—	~1	—	—	53 (5)	—	~1	—	—

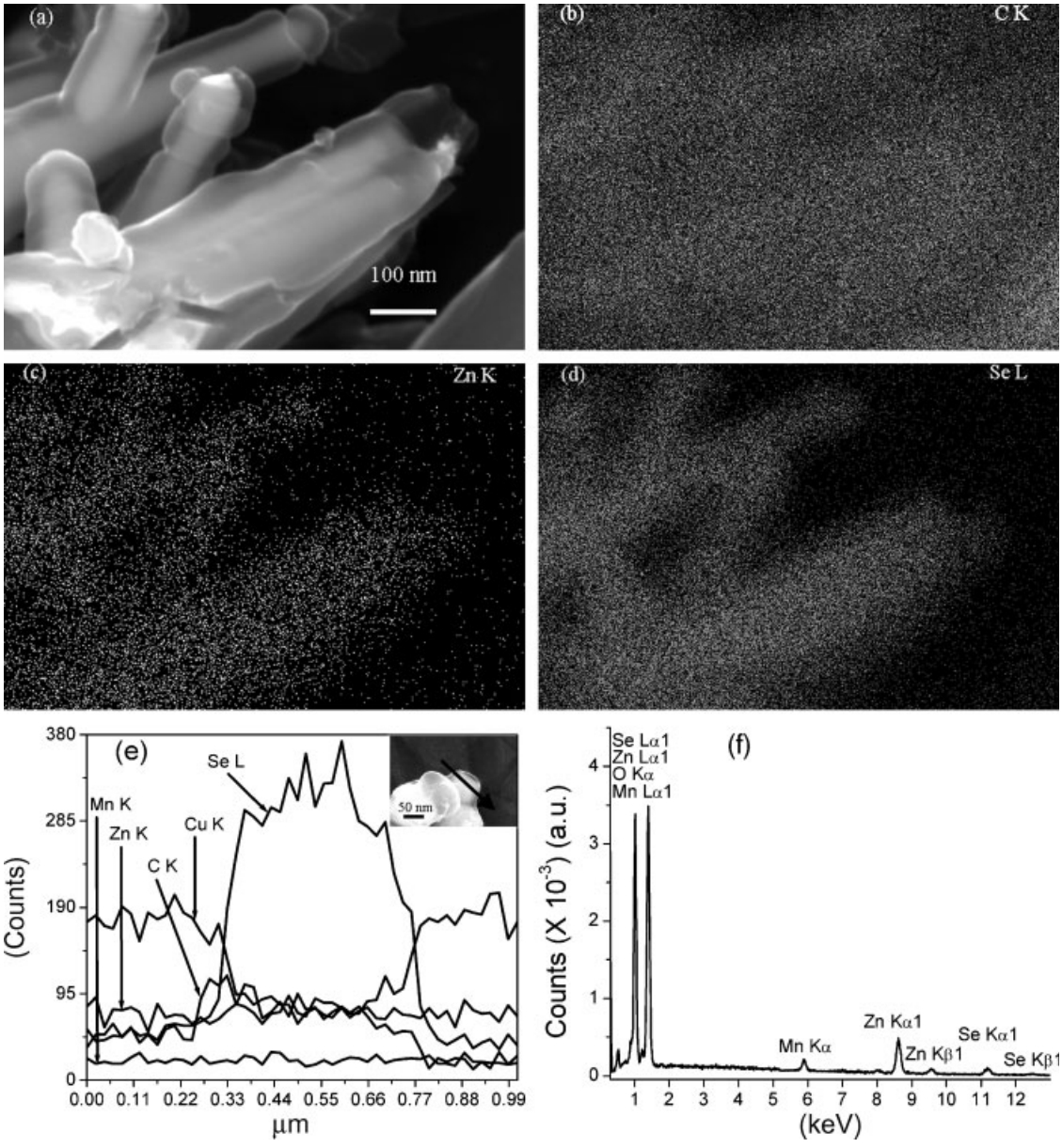

Figure 3. a) Selected area of ZM0 for X-ray elemental dot mapping: b) C, c) Zn, d) Se. e) Elemental line scan of a nanoparticle of ZM1 as indicated by the arrow in inset. f) Bulk WDX spectrum of ZM3.

ADVANCED FUNCTIONAL MATERIALS

spheres are composed of only carbon, as will be demonstrated later, and are present in all the products. As the Mn/Zn atomic ratio increases to 1:20 (ZM2), nanowires of very high *AR* (175) are obtained, as presented in Figure 2d and e. For a 1:10 Mn/Zn ratio (ZM3), several nanorods were observed lying together, sticking onto a carbon microsphere, forming a huge spherical structure with a radius of 3.3 μm (Fig. 2f). The nanorods have an *AR* of 2.2 (Fig. 2g). The *AR* becomes ~1 for the nanostructures in ZM4, where nearly spherical nanoparticles are seen lying scattered within the encapsulating network of amorphous carbon layers, similar to insects being trapped in a spider web. Interestingly, from the SEM/HRSEM images, a pattern for the change in *AR* of the nanostructures with the change in Mn content is observed. *AR* increases from ZM0 to ZM1, increases drastically for ZM2 and then decreases again gradually for the higher Mn contents. Thus, the formation of 1D nanowires is most favored for the Mn/Zn atomic ratio of 1:20 (ZM2).

The precise content of the nanorods in ZM0 was confirmed by employing highly sensitive wave-dispersive X-ray analysis (WDX). The ZM0 sample was mounted on the carbon tape, which was attached to the copper plate. The selected area for the elemental dot mapping (WDX) is shown in Figure 3a. The contents of C, Zn, and Se are presented in Figure 3b–d, respectively. The Zn and Se signals are detected within the position of the nanorods. The C signal is observed around the nanorods, since the C shell encapsulates the nanorod structures. The C signal from outside the nanorods is due to the carbon tape. In order to investigate the core/shell structure, the elemental line scanning of a single nanoparticle in ZM1 (placed on the copper plate) is shown in Figure 3e. As expected, the intensity of the Cu line drops in the sample region. The C line shows a small hump at the left edge of the nanoparticle, which is due to an excess of carbon at the shell of the nanoparticle. As compared to Se, which shows a huge rise in concentration within the nanoparticle, the Zn and Mn signals are sufficiently weak. Although the ratio of Zn/Se is approximately 1, the weaker Zn signal, as compared to the Se signal within the nanoparticle region, is due to the existence of a considerable amount of Zn in the copper plate. Therefore the change in the Zn concentration from the base plate to the nanorod is not as distinct as that of Se. The bulk WDX of ZM3 is shown in Figure 3f. From the observed WDX spectrum, the weight percentage of carbon in the sample is found to be 34 ± 0.4 wt%, and the Mn/Zn and Se/(Zn + Mn) atomic ratios are 10 ± 0 and 48 ± 0 wt%, respectively. The 34 wt% of carbon in ZM3 is composed of the carbon at the shell of the $Zn_{1-x}Mn_xSe$ nanorods aswell as the C microspheres. The micrometer-sized C spheres are shown in Figure 4. The size of the C spheres ranges between 1.5–6 μm. The WDX analysis of a 4.4 μm sphere placed on the copper plate shows only carbon, with no trace of any other element. In the inset in Figure 4, carbon microellipsoids are observed to coexist with the microspheres. Similar ellipsoids have never been observed before, neither in our RAPET studies nor in other carbon structures. The microellipsoids are about 5 μm in breadth and

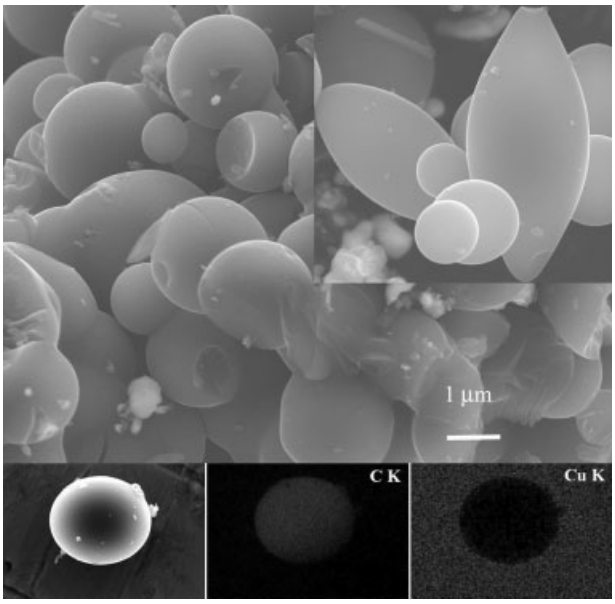

Figure 4. Top) The carbon microspheres in ZM3. Inset) The carbon microellipsoids. Bottom) X-ray dot mapping for C and Cu (from the sample substrate) on a selected C sphere (shown in leftmost image).

12 μm in length. The presence of C shells and C microspheres in the products resulted in a Brunauer–Emmett–Teller (BET) surface area of 6.8–13.3 $m^2\ g^{-1}$ and a pore volume of $0.014 \pm 0.004\ cm^3\ g^{-1}$.

The TEM/HRTEM images in Figure 5 corroborate the morphologies observed in the SEM/HRSEM images in Figure 2. A single nanorod in ZM0 is observed in Figure 5a. The core/shell structure is clearly visible in Figure 5b, and the electron diffraction pattern shows the typical zinc blende reflections of ZnSe (JCPDS card no. 37-1463) in Figure 5c. The C-shell thickness is observed to vary along the circumference. The *AR* of the nanorods of ZM1 as observed from the TEM image of Figure 5d is 1.4 (Table 1). The C shell observed in Figure 5e is 21.0 (±0.4) nm. The HRTEM image of the nanorod core (Fig. 5f) of the ZM1 product further verifies identification of the nanocrystalline zinc blende phase with a perfect arrangement of the atomic layers. The distance measured between the (111) lattice planes is 0.327 nm (as shown with arrows in Fig. 5f), which agrees well with JCPDS card no. 37-1463. The randomly oriented nanowires of ZM2 are observed in Figure 5g. The full length of the nanowires is not visible in the picture; we observed very few with $L = 550$ nm, and the majority of them had $L > 1.4$ μm. A careful observation of the nanowires reveals the C shell with a lighter contrast. The distance between the lattice planes within the nanowires is 0.327 nm (shown with arrows in Fig. 5h) and the nanowires are found to grow in the [111] direction. In ZM3 (Fig. 5i), the *AR* of the observed nanorod is 4.6. Figure 5j shows the tip of a nanorod in ZM3, with a distinct core/shell structure. The HRTEM image of this nanorod (Fig. 5k) shows the C shell to be 12 nm, and the lattice planes of the $Zn_{1-x}Mn_xSe$ core are

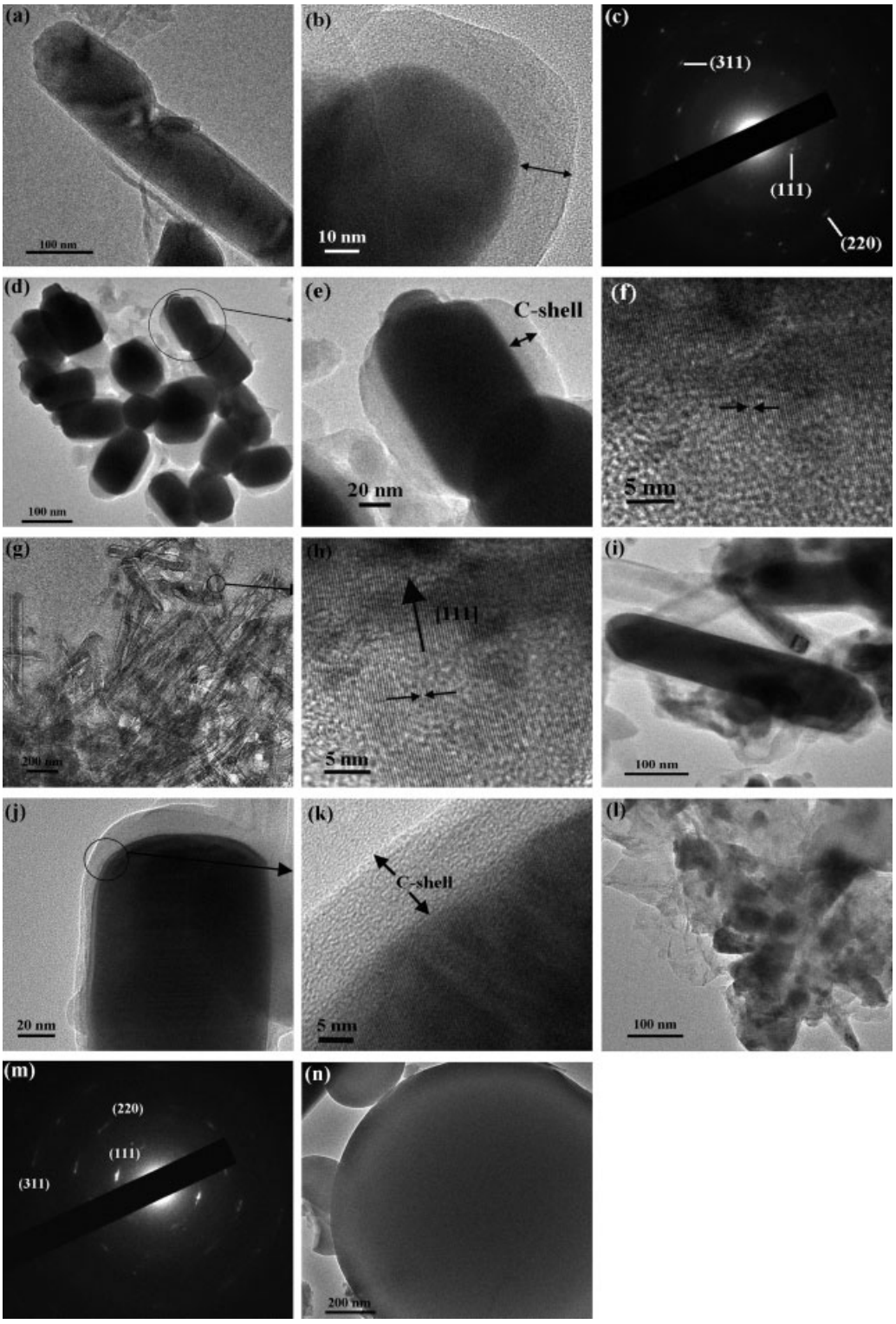

Figure 5. a) Bright-field TEM image of a single nanorod of ZM0; b) the core/shell structure (arrow showing the C shell) in ZM0; c) selected-area electron diffraction pattern (SAED) of ZM0; d) nanorods of ZM1; e) enlarged view of a single core/shell nanorod of ZM1; f) HRTEM image of a nanorod in ZM1; g) the randomly oriented nanowires of ZM2; h) HRTEM image of a single nanowire of ZM2; i) the nanorods of ZM3; j) enlarged view of a single core/shell nanorod of ZM3; k) HRTEM image shows the C shell and the lattice fringes of the nanorod in (j); l) nanoparticles embedded in a C matrix in ZM4; m) electron diffraction pattern of ZM4; and n) carbon microsphere in ZM3.

ADVANCED FUNCTIONAL MATERIALS

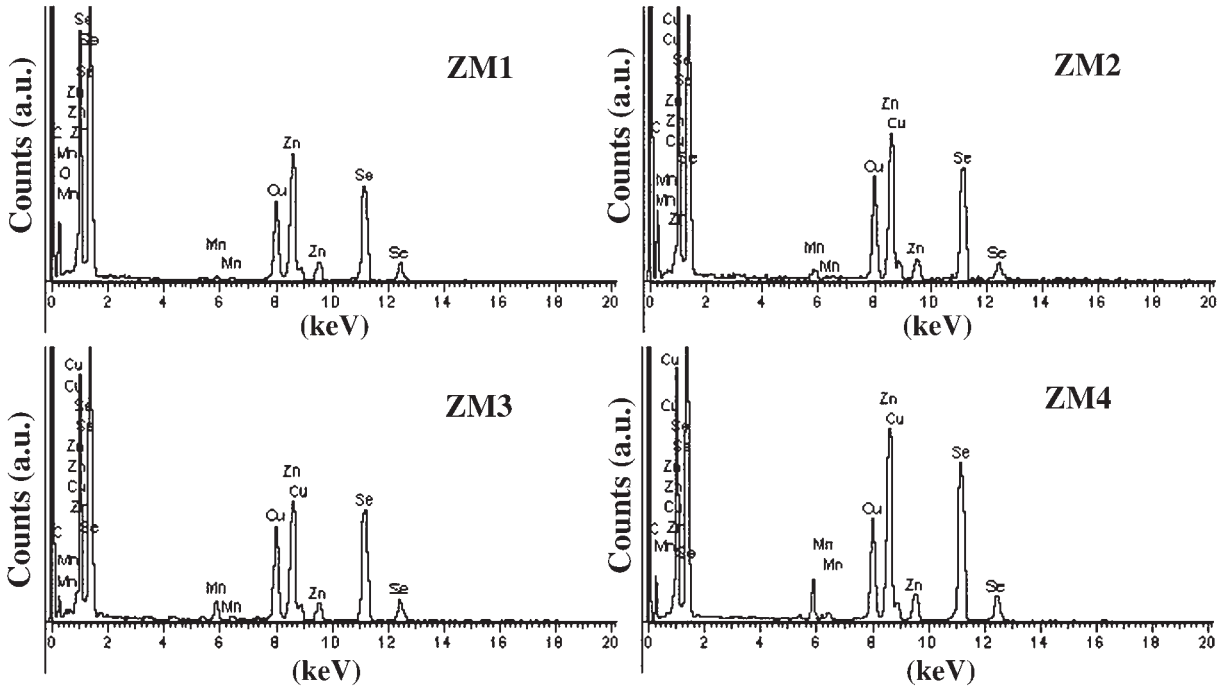

Figure 6. The EDS results for $Zn_{1-x}Mn_xSe$@C products of varying Mn/Zn atomic ratio.

0.327 nm apart from each other. The partially ordered lattice planes of carbon around the dark core have an interlayer spacing of approximately 3.67 Å, which is slightly larger than that for graphitic layers. The TEM image of ZM4 in Figure 5l mirrors the SEM image (Fig. 2h). The electron diffraction pattern of this region (Fig. 5m) shows typical reflections of the zinc blende $Zn_{1-x}Mn_xSe$ phase. A C microsphere having $D = 1.2$ μm is shown in the TEM image of Figure 5n.

The results obtained from energy dispersive X-ray spectroscopy (EDS) coupled with TEM are shown in Figure 6. The EDS spectra were recorded at five or six different locations of the Cu grids to ascertain the homogeneity of the Mn incorporation in the nanocrystals. The Mn/Zn atomic ratios obtained from the EDS results are 0.01(0), 0.05(0), 0.11(0), and 0.19(0) for ZM1, ZM2, ZM3, and ZM4, respectively. These values match well with the quantitative analysis by ICP measurements. Thus, from the observed SEM/HRSEM and TEM/HRTEM images, we can conclude the following: a) the *AR* of the nanostructures varies thus: 4.5, 1.8 (1.4), 175, 2.2 (4.6), and 1, as the Mn/Zn atomic ratio increases through these corresponding values 0, 1:100, 1:20, 1:10, and 1:5; b) there is a large size distribution in the nanostructures; c) the carbon forms the nonuniform shell over the $Zn_{1-x}Mn_xSe$ core, and 10–20 nm thick amorphous carbon layers completely encapsulate the $Zn_{1-x}Mn_xSe$ core; d) Mn or MnSe phases were not detected and hence these phases are absent; e) C microspheres are present as separate entities alongside the $Zn_{1-x}Mn_xSe$@C nanostructures.

The EPR experiments on the carbon-encapsulated products are consistent with Mn embedded inside the host lattice. EPR spectra can be used to determine the location of Mn. For ZM0, an EPR signal was not observed, which indicates the absence of any recombination center at the Zn vacancies in ZnSe@C at 300 K. Also, the paramagnetic centers of the carbon shell are not observed.[18] In the Mn-doped products, the hyperfine interaction with the ^{55}Mn nuclear spin ($I = 5/2$) at 300 K gives rise to the six line spectra,[5b,19] which is also observed in our case. From Figure 7, we determine a hyperfine splitting of $60.9 \times 10^{-4}\,cm^{-1}$ for ZM1 at 300 K. This value agrees well with that obtained for Mn at cubic lattice sites in bulk ZnSe [$(60.4 \times 10^{-4}\,cm^{-1})$[5a] and $(60.9 \times 10^{-4}\,cm^{-1})$[20]]. It has been observed previously that with an increase in Mn concentration, Mn segregates at the surface of the nanocrystal.[20,21] However, in our case, even with quite a high Mn doping of 1:20, 1:10, and 1:5, Mn still occupies the Zn sites in the $Zn_{1-x}Mn_xSe$ lattice. The hyperfine splitting is still observed for ZM2, ZM3, and ZM4, with the hyperfine splitting constants at 62.9×10^{-4}, 56×10^{-4}, and $55.5 \times 10^{-4}\,cm^{-1}$, respectively, at 300 K. According to earlier reports, increased Mn concentration led to enhanced hyperfine splitting magnitudes, implying reduced covalency and less coupling between the ground state of Mn and sp-states of the nanocrystals.[20–22] In our case, the hyperfine splitting values decrease with increase in Mn concentration. However, for ZM2, ZM3, and ZM4, the symmetry of the six-line spectra is hindered by a sharp absorption line at the center. The dipole–dipole interactions between the Mn impurities (Mn–Mn exchange interactions) give rise to a broadening with poor resolution and a broad background signal.[21] Mn has a tendency to form pairs and clusters with an increase in the number of Mn atoms, and

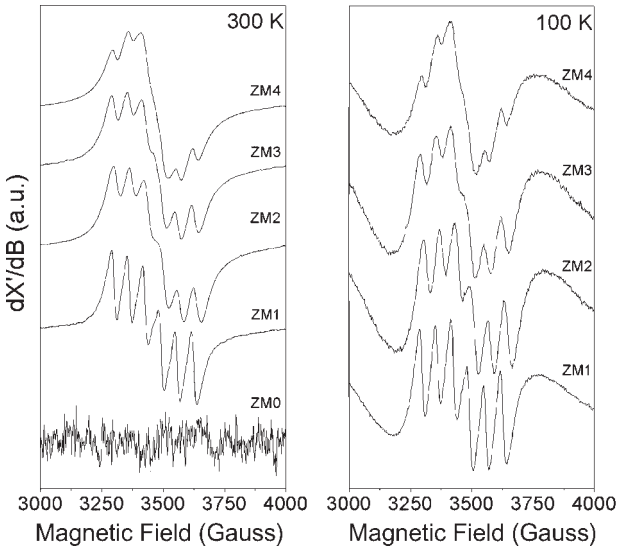

Figure 7. EPR spectra, at 300 K and 100 K, showing the hyperfine splitting in carbon-encapsulated pristine and Mn-doped ZnSe samples.

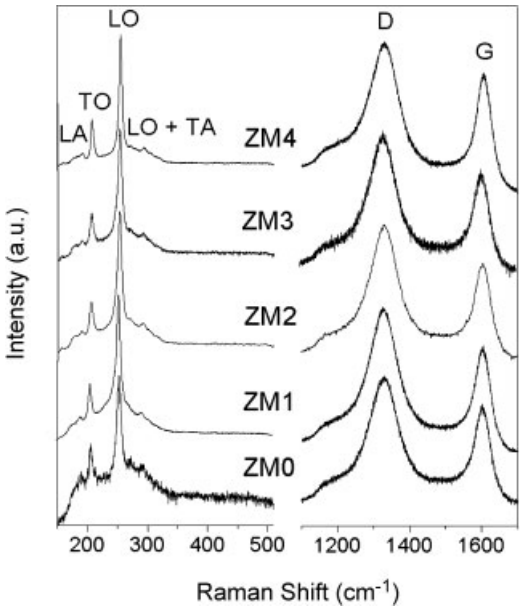

Figure 8. Raman spectra of the $Zn_{1-x}Mn_xSe$@C products.

reduces the hyperfine interactions.[20,21] The temperature of the EPR experiments (300 K) was high enough to properly resolve the forbidden and allowed hyperfine transitions. The EPR experiments at 100 K, did not improve the spectra sufficiently, except that the hyperfine splitting is slightly increased. At 100 K, the hyperfine splitting values are 61.4×10^{-4}, 56.2×10^{-4}, 56.1×10^{-4}, and 54.9×10^{-4} cm^{-1} for ZM1, ZM2, ZM3, and ZM4, respectively. Hence, it cannot be ruled out that the EPR signals of Mn^{2+} arise from different environments, that is, a distribution between the bulk and surface of the nanocrystals, and this distribution is expected to increase with an increase in Mn content. The corresponding trend is obvious in Figure 7 as the underlying broad signal increases in signal strength compared to the six-line hyperfine spectra. However, based on this result it is clear that the total Mn content in ZM4 (Mn/Zn atomic ratio = 0.199), as determined by ICP analysis, is actually a reflection of a hybrid, that is, Mn present and attached to the carbon shell, central core region, and the surface of the nanocrystal. This is possible since the 53–55 nm ZM4 nanocrystals show bulk-like behavior. The characterization techniques such as XRD, EPR, and Raman spectroscopy mainly probe the central core region of the ZM4 nanocrystal, where the maximum Mn content is probably approximately 10% or at least considerably below that measured by ICP analysis. This is quite obvious since the EPR spectra of the II–VI DMS compounds with 20% Mn should not show a hyperfine structure anymore, and should consist only of a single exchange-broadened Lorentzian band.[23] The reason that we observe a hyperfine structure for ZM4 is because of the approximate 10% Mn content of the central core region.

Figure 8 shows the room-temperature Raman spectra of the products, where 150–500 cm^{-1} and 1100–1700 cm^{-1} correspond to the spectral regions of the $Zn_{1-x}Mn_xSe$ core and carbon shell, respectively. The Raman peaks are observed at 190, 206, 254, 292, 1330, and 1600 cm^{-1}. The Raman peaks at 206 and 254 cm^{-1} are attributed to the transverse optic (TO) and longitudinal optic (LO) phonon modes of ZnSe. For ZnSe nanobelts and nanowires, the TO phonon modes have been observed at 203–205 cm^{-1},[2a,c] whereas the LO phonon frequencies have been observed at 254 and 255 cm^{-1} for single-crystalline ZnSe.[4b] The very weak peaks at 190 and 292 cm^{-1} are attributed to longitudinal acoustic (LA) and LO + TA (transverse acoustic) multiphonon modes of ZnSe.[24] The splitting between the LO and TO phonon modes increases by 2.6 cm^{-1} because of the shift of the LO and TO phonon modes with the increase in the Mn concentration from ZM0 to ZM4. The observed splitting is much smaller than the previously reported LO–TO splitting of about 10 cm^{-1} for a Mn content of 20%;[25] probably this is due to a lesser amount of Mn in the central core region of the ZM4 nanocrystal and also the effect of the encapsulating carbon shell on the phonon modes of the $Zn_{1-x}Mn_xSe$ core. However, additional peaks were not observed because of the impurity mode of Mn in ZnSe. The relatively sharp and symmetric Raman peaks suggest that the $Zn_{1-x}Mn_xSe$ nanostructures are highly crystalline and single phase, which is in accord with the HRTEM observations shown above. The Raman spectrum in the region 1100–1700 cm^{-1} is characteristic of disordered graphitic carbon.[26] The Raman peaks at 1330 and 1600 cm^{-1} are the D- and G-bands. The D-band is attributed to the Raman-inactive A_{1g} vibration mode assigned to the vibrations of carbon atoms with dangling bonds in planar terminations of disordered graphite.[27] The G-band is the Raman active optical mode E_{2g} of 2D graphite, which is closely related to the vibrations in sp^2-bonded carbon atoms.[28] The C shell

encapsulating the $Zn_{1-x}Mn_xSe$ core might be disordered as the reaction temperature (800 °C) is not high enough to improve the local order of the formed carbon layers.

Unlike our assumption that the C shell will absorb the emitted radiation and luminescence will not be observed, significant luminescence was observed in the $Zn_{1-x}Mn_xSe$@C products. In order to examine the temperature dependence of the luminescence for various Mn-doping concentrations, we performed CL spectroscopy for temperatures ranging from 62 to 300 K. The electron beam (e-beam) was raster-scanned over an area of 256 μm × 192 μm for each sample to yield an effective spatial average of the CL spectra for this area. The CL results are qualitatively similar to a previous photoluminescence study that was performed for ZnSe nanocrystals doped with much lower Mn concentrations, ranging from 0.2 to 0.9%.[9] Stack plots of CL spectra are shown in Figure 9 for all five samples, with the peak heights for each group of spectra normalized according to scaling factors, as indicated. Distinct emission in the wavelength range of 430 to 470 nm is attributed to the ZnSe near-bandgap excitonic recombination. Typical red-shifts of 20–25 nm are observed as the temperature is raised from 62 to 300 K, consistent with the expected temperature dependence of the ZnSe bandgap. The emissions centered at about 575 nm in Figure 9b are attributed to the $^4T_1$-to-$^6A_1$ transition of the Mn^{2+} ion in a ZnSe crystal.[29] The broad and intense Mn-related emission is a strong indication that Mn is well-incorporated both structurally and electronically into the ZnSe host crystal. In Figure 9a, various structures are observed towards longer and shorter wavelengths of the ZnSe near-band-edge emission. Emission towards longer wavelengths is attributed to the presence of a defect, impurity, and possibly surface recombination that becomes more prominent at the lower temperatures. A shoulder on the shorter wavelength (higher energy) side of the ZnSe emission is also observed in samples ZM1, ZM2, and ZM3. We attribute these components as being due to excitation of smaller nanocrystals within the ensemble of nanowires, nanorods, and nanoparticles that give rise to a quantum size effect. The disappearance of these higher energy peaks at higher temperatures may reflect an enhanced nonradiative recombination rate for smaller

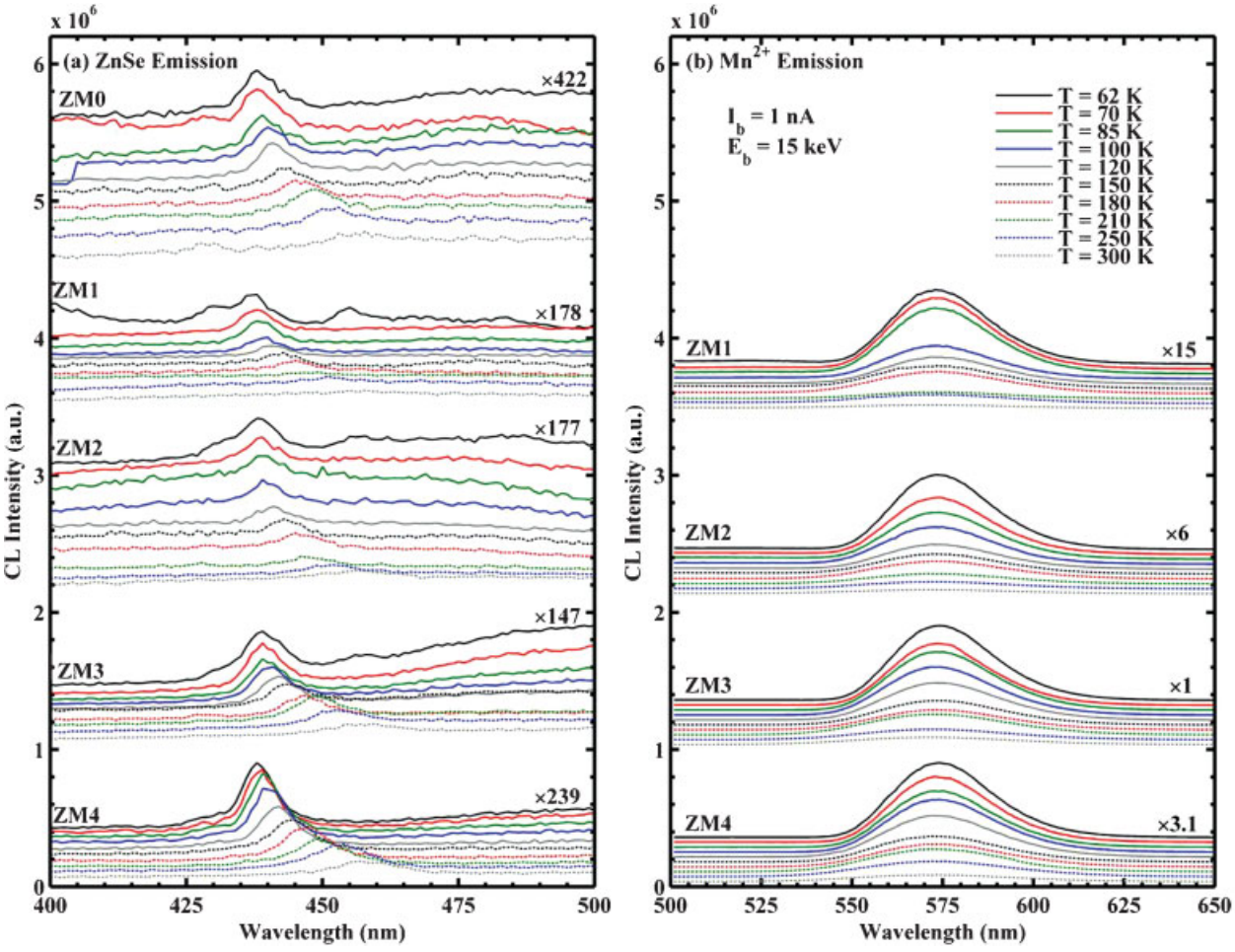

Figure 9. Spatially averaged CL spectra for all ZnSe:Mn^{2+} samples in the 400 to 500 nm range, showing the ZnSe near-band-edge emission, and the 500–650 nm range, representing the Mn-related emission. Scale factors located next to each group of spectra indicate the multiplicative scaling of each group relative to the Mn-related emission of sample ZM3, which exhibited the most intense emission.

nanoparticles at higher temperatures relative to that for the larger nanoparticles that emit closer to the ZnSe bandgap energy.

Evidence for the presence of nonradiative recombination was acquired by examining the dependence of the ZnSe near-band-edge emission on the time of exposure to the electron beam, which had a beam current of 1 nA and beam energy of 15 keV. The CL intensity of the ZnSe emission for all samples was found to decrease by a factor of about 10 during exposure to the e-beam for about 1 min, after which the CL intensity was found to saturate at a roughly fixed intensity, independent of the time of the remaining exposure. Such a decrease in CL intensity can be explained by disruption of the ZnSe core and graphitic carbon shell bonds, as a result of the high-energy e-beam injection. Due to the disordered nature of the shell, we hypothesize that such an e-beam exposure will induce defects, changes, or disruptions in such bonding, resulting in an increase in nonradiative recombination centers at the core/shell interface that are responsible for a decrease in the efficiency of luminescence with exposure time. Thermally activated nonradiative recombination is also ostensibly present, as evidenced by a decreased CL intensity for both the ZnSe- and Mn-related emissions as the temperature is increased from 62 to 300 K, as observed for each group of spectra in Figure 9a and b.

The intensity of the Mn-related emission is roughly proportional to its concentration in the ZnSe nanocrystals, as shown in Figure 10. The CL intensity ratio of the Mn- and ZnSe-related emissions, I_{Mn}/I_{ZnSe}, is shown for each sample as a function of temperature. The reduced intensity ratio of ZM4 relative to that for ZM3 may indicate a reduced relative incorporation of Mn into the ZnSe host-lattice for alloy concentrations higher than approximately 10% in this preparation. It is also apparent from both sets of spectra in Figure 9a and b, when considering the scale factors, that the total efficiency of luminescence for sample ZM3 is greater than that for ZM4 by a factor of about 3, again suggesting a larger density of nonradiative defects in ZM4 relative to that for ZM3.

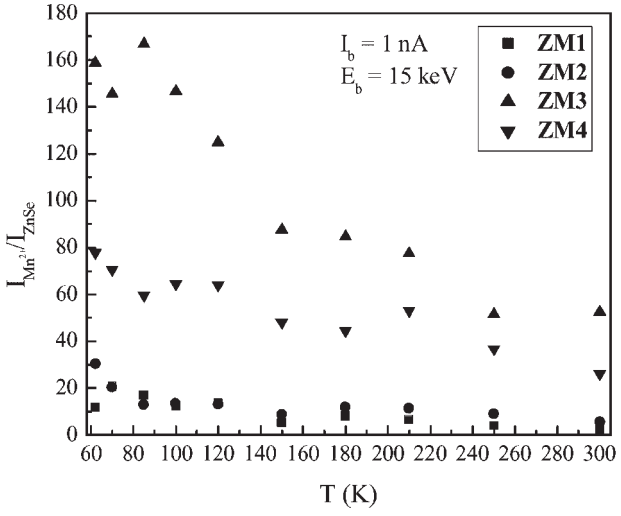

Figure 10. CL peak intensity ratio, I_{Mn}/I_{ZnSe}, of the Mn-related emission to the ZnSe near-band-edge emission as a function of temperature.

Based on the above HRSEM and TEM/HRTEM results, a formation mechanism is proposed for the $Zn_{1-x}Mn_xSe$@C nanostructures. Three basic observations lead to the proposed mechanism. Firstly, carbon formed a shell over the $Zn_{1-x}Mn_xSe$ nanostructures; secondly, for ZM0 (ZnSe without any Mn), nanorods were observed without any external template or catalyst (hence, it must be a self-catalyzed growth); and thirdly, the *AR* of the nanostructures varied with the Mn concentration, which means that the Mn within the $Zn_{1-x}Mn_xSe$ lattice has a role to play in the growth of the nanowires and nanorods. When heated to 800 °C inside the Swagelok reactor, the Zn and Mn acetates decompose into their gaseous state along with gaseous selenium (boiling point of Se is 685 °C). According to the previous report, all the products of the dissociation reaction, in a closed Swagelok reaction, float in the gas phase and solidify right after their formation.[30] The dissociation of acetates involves the following steps:[31]

$$M(CH_3COO)_2 \cdot xH_2O \rightarrow M(CH_3COO)_2 + xH_2O \quad (M = Zn,\ Mn) \tag{1}$$

$$M(CH_3COO)_2 \rightarrow MCO_3 + CH_3COCH_3 \tag{2}$$

$$CH_3COCH_3 \rightarrow CO + C_2H_6 \tag{3}$$

$$2CO \rightarrow C + CO_2 \quad \text{(Boudouard reaction)} \tag{4}$$

$$MCO_3 \rightarrow MO + CO_2 \tag{5}$$

$$MO + CO \rightarrow M + CO_2 \quad \text{(does not occur)} \tag{6}$$

The metal carbonate, which is a short-lived intermediate, immediately decarboxylates to give a metal oxide at 350 °C.[31] However, the carbon monoxide and carbon, formed from Equations 3 and 4, respectively, cannot reduce the metal oxides as the standard reduction potential values at 25 °C for Zn and Mn are −0.76 and −1.18 V, respectively.[32] Hence, the reactions according to Equation 6 do not occur and $(Zn_{1-x}Mn_x) - O$ is formed according to Equation 5. To confirm this fact, control reactions were carried out at 800 °C for 12 h. In the first we reacted Zn acetate and in the second Mn acetate, both reactions in the absence of Se. ZnO and MnO were the final products for each of the individual reactions, instead of metallic Zn and Mn, respectively. Selenium evaporates above 685 °C and reacts with $(Zn_{1-x}Mn_x) - O$ to form $Zn_{1-x}Mn_xSe$ via the following reaction: 2 $Zn_{1-x}Mn_x O + 2\ Se \rightarrow 2\ Zn_{1-x}Mn_xSe + O_2$. ZnSe was previously synthesized from ZnO and Se, in an organic, solvent-mediated reaction.[3b] A little stoichiometric excess of Se was required in our case as a lesser amount of Se and a temperature below

ADVANCED FUNCTIONAL MATERIALS

800 °C retained a small amount (<10 wt%) of a $Zn_{1-x}Mn_xO$ impurity phase along with $Zn_{1-x}Mn_xSe$. The formation of the carbon shell over the semiconducting core is a kinetically controlled process.[33] The solidification rate of $Zn_{1-x}Mn_xSe$ is faster than carbon, and hence, $Zn_{1-x}Mn_xSe$ crystallizes initially, followed by carbon, giving rise to the core/shell structure.

To eliminate the possibility of any catalytic reaction by Fe, Co, Ni, or Cr (Swagelok body components) in the formation of the nanowires and nanorods, control experiments were carried out in which a quartz tube was filled with the reactants. The quartz tube was placed inside the Swagelok reactor. No change was observed in the composition, structure, or morphology of the products. This confirms that the Swagelok body has no catalytic role. The template-free and catalyst-free formation of nanorods for ZM0 (pristine ZnSe) can be attributed to a proposed kinetically controlled growth process. As schematically represented in Figure 11a, when a ZnSe nucleus is formed, the disordered graphitic carbon starts encapsulating the nucleus. The second ZnSe nucleus can only join the first one in one direction, where the encapsulating shell is not yet formed. The carbon is continuously supplied, the formation of the carbon sheet continues, and there is a gradient in the carbon density. At this juncture, it is important to note that the inhomogeneous coating of a few nanocrystals with the carbon shell (Figs. 3e, 5d and e), might result if the gradient in the carbon density is not uniform during the core/shell formation process. The carbon continues encapsulating the new nucleus, leaving one position that the next ZnSe nucleus can join. Hence, in due course, the ZnSe core grows in one direction, preventing an isotropic growth because of the encapsulating carbon shell around the core. Once no more ZnSe nuclei are added, the carbon finally encapsulates the core completely. This leads to the formation of the ZM0 core/shell nanorods. The growth process of the nanorods is not uniform, leading to a large size distribution in the nanorods.

Although the same proposed growth mechanism applies to the Mn-doped ZnSe products, manganese can further catalyze and accelerate the formation of the 1D nanostructures.[34] Thus, Mn alters the *AR* of the nanorods and nanowires. For the growth of nanowires, the solid catalytic particle is generally located at the tip of the nanowire, and serves as the seed for nanowire growth.[35] Since all the Mn is inside the $Zn_{1-x}Mn_xSe$ lattice, there is no free metallic Mn nanoparticle to serve as the seed for nanowire/nanorod growth, and hence, the Mn embedded inside the lattice is likely to serve as the catalyst. The one-dimensional growth of nanowires (for ZM2) in the [111] direction (Fig. 5h) and the dependence of *AR* on Mn concentration implies that Mn^{2+} replaces the Zn^{2+} ions mainly in the (111) plane in the $Zn_{1-x}Mn_xSe$ lattice. This fact is also evidenced from the shift of the (111) XRD reflection with increasing Mn concentration (Fig. 1). The $Zn_{1-x}Mn_xSe$ crystal structure is formed during the kinetically controlled solidification of the gaseous mixture. The sequential formation of the $Zn_{1-x}Mn_xSe$ nucleus and the encapsulation by carbon occurs simultaneously with the addition of other nuclei, in the formation of a 1D structure, similar to the formation of ZM0 nanorods (discussed previously). However, Mn on the (111) plane of the zinc blende lattice accelerates the growth of the nanowires in ZM2 (Fig. 11b). For ZM1, the amount of Mn is low. For ZM2, Mn concentration is optimum for Mn^{2+} to replace Zn^{2+} along the (111) plane (i.e., along the nanowire length), and the nanowires grow to their maximum length ($AR = 175$). For higher Mn concentrations (ZM3 and ZM4), Mn^{2+} replaces Zn^{2+} on other planes in addition to the (111) plane. The unidirectional growth is hindered (tending towards isotropic growth), since Mn on other lattice planes tries to direct the nanostructure growth to their respective directions (Fig. 11c). Hence, for ZM3, the *AR* decreases, and for ZM4, nearly spherical nanoparticles are formed.

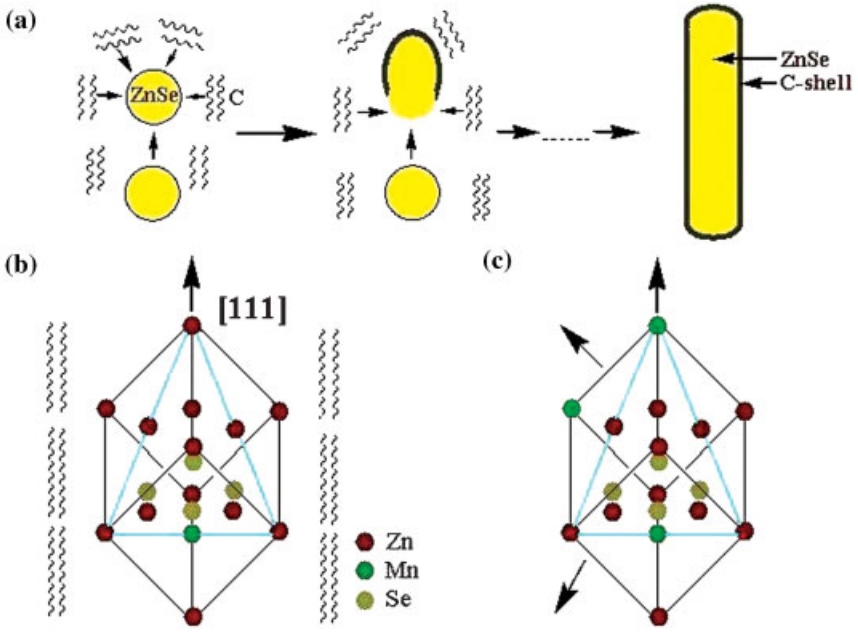

Figure 11. a) Schematic representation for formation of nanorods in ZM0. The position of Mn in the crystal lattice of b) ZM2 and c) ZM4. The arrows indicate the growth direction.

3. Conclusions

In conclusion, carbon-encapsulated $Zn_{1-x}Mn_xSe$ nanowires, nanorods and nanoparticles were synthesized by the solvent-free, one-step reactions under autogenic pressure at elevated temperature approach. The aspect ratio of the nanowires/nanorods varied from 4.5, to 1.8, to 175, to 4.6, and to 1, as the Mn/Zn atomic ratio increased from 0, to 1:100, to 1:20, to 1:10, and finally

to 1:5, respectively. A 10–20 nm thick amorphous carbon shell was measured from HRSEM and HRTEM analysis. EPR measurements indicated that Mn replaced Zn in the $Zn_{1-x}Mn_xSe$ lattice and was not present on the surface of the nanocrystal or in the surrounding matrix. CL experiments in the temperature range 62–300 K revealed ZnSe near-bandgap excitonic recombination and the $^4T_1$-to-$^6A_1$ transition of the Mn^{2+} ion in the ZnSe host lattice. The reduced intensity ratio (I_{Mn}/I_{ZnSe}) of ZM4 relative to that for ZM3 indicated a reduced relative incorporation of Mn into the ZnSe host lattice for Mn concentrations higher than about 10%. The mechanism for the formation of the core/shell nanowires and nanorods, without the use of any template or structure-directing agent, was explained based on a kinetically controlled process of the $Zn_{1-x}Mn_xSe$ nucleus formation and subsequent carbon encapsulation. Mn embedded in the ZnSe lattice directed the nanowire growth in a [111] direction. The $Zn_{1-x}Mn_xSe$@C nanostructures are eligible for biological applications because of the C shell, which eliminates toxic effects.

4. Experimental

Zinc acetate dihydrate ($C_4H_6O_4Zn \cdot 2H_2O$, Acros Organics, 98%), manganese(II) acetate tetrahydrate ($C_4H_6O_4Mn \cdot 4H_2O$, Fluka, >99%) and selenium powder (100 mesh, Aldrich, 99.99%) were used as received. In a typical synthesis of Mn-doped ZnSe nanostructures coated with carbon, 1 g of $C_4H_6O_4Zn \cdot 2H_2O$, 0.9 g of Se, and a stoichiometric amount of $C_4H_6O_4Mn \cdot 4H_2O$ (according to the Mn/Zn atomic ratio of 0, 1:100, 1:20, 1:10, or 1:5) were mixed and introduced into a 2 mL stainless steel Swagelok reactor at room temperature. The filled reactor was tightly closed and placed at the center of the tube furnace. The temperature of the furnace was raised to 800 °C at a rate of 10 °C min^{-1} and the temperature was maintained for 12 h. The reactor was gradually cooled (over about 5 h) to room temperature and opened. The yield of gray-colored $Zn_{1-x}Mn_xSe$@C product was 70.5%.

The obtained products were structurally characterized by using the following techniques: HRSEM (JSM, 7000F), low- and high-resolution TEM (JEOL, 2010), powder XRD (Cu Kα = 1.5418 Å radiation, Bruker AXS D8), inductively coupled plasma atomic emission spectroscopy (Spectroflame Module E), wave-dispersive X-ray (JSM, 7000F; coupled to the HRSEM instrument), and energy dispersive X-ray (JEOL, 2010; coupled to HRTEM) spectroscopies. A Micrometrics (Gemini 2375) surface area analyzer was used to measure the surface area of the products at liquid-nitrogen temperature (−196 °C). The EPR spectra were recorded on a Bruker EPR spectrometer (ER083 CS) operating at an X-band (ν = 9.77 GHz) with a 100 kHz magnetic-field modulation. An Olympus BX41 (Jobin–Yvon–Horiba) Raman spectrometer was employed, using the 514.5 nm line of an Ar-ion laser as the excitation source to analyze the nature of the core as well as that of the carbon shell. The CL experiments were performed with a modified JEOL-5910 scanning electron microscope using a 15 keV electron beam with a probe current of 1 nA. A UV multialkali photomultiplier tube (PMT) operating in the 185 to 850 nm spectral range enabled photon counting of the luminescence that was dispersed by a 0.25 m monochromator. Measurements were performed at different temperatures in the 62 to 300 K temperature range [36].

Received: June 14, 2007
Revised: December 23, 2007
Published online: May 20, 2008

[1] a) Q. Li, X. Gong, C. Wang, J. Wang, K. Ip, S. Hark, *Adv. Mater.* **2004**, *16*, 1436. b) A. B. Panda, S. Acharya, S. Efrima, *Adv. Mater.* **2005**, *17*, 2471.

[2] a) Z. D. Hu, X. F. Huan, M. Gao, Q. Chen, L.-M. Peng, *J. Phys. Chem. C* **2007**, *111*, 2987. b) X. Zhang, Z. Liu, Q. Li, Y. Leung, K. Ip, S. Hark, *Adv. Mater.* **2005**, *17*, 1405. c) Y. Jiang, X.-M. Meng, W.-C. Yiu, J. Liu, J.-X. Ding, C.-S. Lee, S. T. Lee, *J. Phys. Chem. B* **2004**, *108*, 2784. d) A. B. Panda, G. Glaspell, M. S. El-Shall, *J. Am. Chem. Soc.* **2006**, *128*, 2790. e) S. Acharya, A. B. Panda, S. Efrima, Y. Golan, *Adv. Mater.* **2007**, *19*, 1105. f) Y. Cai, S. K. Chan, I. K. Sou, Y. F. Chan, D. S. Su, N. Wang, *Adv. Mater.* **2006**, *18*, 109. g) S. Xiong, J. Shen, Q. Xie, Y. Gao, Q. Tang, Y. Qian, *Adv. Funct. Mater.* **2005**, *15*, 1787.

[3] a) J. Zhu, Y. Koltypin, A. Gedanken, *Chem. Mater.* **2000**, *12*, 73. b) H.-S. Chen, B. Lo, J.-Y. Hwang, G.-Y. Chang, C.-M. Chen, S.-J. Tasi, S.-J. J. Wang, *J. Phys. Chem. B* **2004**, *108*, 17 119.

[4] a) Q. Peng, Y. Dong, Y. Li, *Angew. Chem. Int. Ed.* **2003**, *42*, 3027. b) W. Yao, S.-H. Yu, J. Jiang, L. Zhang, *Chem. Eur. J.* **2006**, *12*, 2066. c) J. Hu, Y. Bando, J. Zhan, Z. Liu, D. Golberg, S. P. Ringer, *Adv. Mater.* **2005**, *17*, 975.

[5] a) D. J. Norris, N. Yao, F. T. Charnock, T. A. Kennedy, *Nano Lett.* **2001**, *1*, 3. b) S. C. Erwin, L. Zu, M. I. Haftel, A. L. Efros, T. A. Kennedy, D. J. Norris, *Nature* **2005**, *436*, 91. c) N. S. Norberg, G. M. Dalpian, J. R. Chelikowsky, D. R. Gamelin, *Nano Lett.* **2006**, *6*, 2887. d) L. Zu, D. J. Norris, T. A. Kennedy, S. C. Erwin, A. L. Efros, *Nano Lett.* **2006**, *6*, 334. e) N. Pradhan, X. Peng, *J. Am. Chem. Soc.* **2007**, *129*, 3339.

[6] I. Žutić, *Nat. Mater.* **2006**, *5*, 771.

[7] J. Y. Lee, D. S. Kim, J. H. Kang, S. W. Yoon, H. Lee, J. Park, *J. Phys. Chem. B* **2006**, *110*, 25 869.

[8] a) C. Jin, B. Zhang, Z. Ling, J. Wang, X. Hou, Y. Segawa, X. Wang, *J. Appl. Phys.* **1997**, *81*, 5148. b) B. Daniel, K. C. Agarwal, J. L. Schomber, C. Klingshirn, M. Hetterich, *Appl. Phys. Lett.* **2005**, *87*, 212 103.

[9] a) J. F. Suyver, S. F. Wuister, J. J. Kelly, A. Meijerink, *Phys. Chem. Chem. Phys.* **2000**, *2*, 5445. b) T. .J Norman, Jr, D. Magana, T. Wilson, C. Burns, J. Z. Zhang, D. Cao, F. Bridges, *J. Phys. Chem. B* **2003**, *107*, 6309. c) J. Lu, S. Wei, Y. Peng, W. Yu, Y. Qian, *J. Phys. Chem. B* **2003**, *107*, 3427. d) H. R. Heulings, IV, X. Huang, J. Li, T. Yuen, C. L. Lin, *Nano Lett.* **2001**, *1*, 521. e) N. Pradhan, D. M. Battaglia, Y. Liu, X. Peng, *Nano Lett.* **2007**, *7*, 312.

[10] P. V. Radovanovic, C. J. Barrelet, S. Gradecak, F. Qian, C. M. Lieber, *Nano Lett.* **2005**, *5*, 1407.

[11] a) J. Xiang, W. Lu, Y. J. Hu, Y. Wu, H. Yan, C. M. Lieber, *Nature* **2006**, *441*, 489. b) S. Kodambaka, J. Tersoff, M. C. Reuter, F. M. Ross, *Science* **2007**, *316*, 729.

[12] a) I. L. Medintz, H. T. Uyeda, E. R. Goldman, H. Mattoussi, *Nat. Mater.* **2005**, *4*, 435. b) C. Kirchner, T. Liedl, S. Kudera, T. Pellegrino, A. M. Javier, H. E. Gaub, S. Stolzle, N. Fertig, W. J. Parak, *Nano Lett.* **2005**, *5*, 331. c) D. Gerion, F. Pinaud, S. C. Williams, W. J. Parak, D. Zanchet, S. Weiss, A. P. Alivisatos, *J. Phys. Chem. B* **2001**, *105*, 17. d) A. Fu, W. Gu, C. Larabell, A. P. Alivisatos, *Curr. Opin. Neurobiol.* **2005**, *15*, 568.

[13] a) S. E. Rodil, R. Olivares, H. Arzate, S. Muhl, *Diamond Relat. Mater.* **2003**, *12*, 931. b) S. Lindera, W. Pinkowskic, M. Aepfelbacherb, *Biomaterials* **2002**, *23*, 767. c) A. Dorner-Reisel, C. Schurer, E. Muller, *Diamond Relat. Mater.* **2004**, *13*, 823. d) V. Stary, L. Bacakova, J. Hornik, V. Chmelik, *Thin Solid Films* **2003**, *433*, 191. e) H. J. Steffen, J. Schmidt, A. Gonzalez-Elipe, *Surf. Interface Anal.* **2000**, *29*, 386. f) T. R. Lawson, S. A. Catledge, Y. K. Vohra, *Key Eng. Mater.* **2005**, *284–286*, 1015. g) I. Dion, C. Baquey, J. R. Monties, *Int. J. Artif. Organs* **1993**, *16*, 623. h) J. Wang, N. Huang, P. Yang, Y. X. Leng, H. Sun, Z. Y. Liu, P. K. Chu, *Biomaterials* **2004**, *25*, 3163. i) L. A. Thomson, F. C. Law, N. Rushton, *Biomaterials* **1991**, *12*, 37. j) D. J. Li, H. Q. Gu, *Bull. Mater. Sci.* **2002**, *25*, 7.

[14] R. S. Ruoff, D. C. Lorents, B. R. Chan, R. Malhotra, S. Subramoney, *Science* **1993**, *259*, 346.
[15] M. Janotta, D. Rudolph, A. Kueng, C. Kranz, H.-S. Voraberger, W. Waldhauser, B. Mizaikoff, *Langmuir* **2004**, *20*, 8634.
[16] B. Y. Geng, Q. B. Du, X. W. Liu, J. Z. Ma, X. W. Wei, L. D. Zhang, *Appl. Phys. Lett.* **2006**, *89*, 033 115.
[17] A. A. Demkov, O. F. Sankey, *Phys. Rev. B* **1993**, *48*, 2207.
[18] O. E. Andersson, B. L. V. Prasad, H. Sato, T. Enoki, Y. Hishiyama, Y. Kaburagi, M. Yoshikawa, S. Bandow, *Phys. Rev. B* **1998**, *58*, 16 387.
[19] A. K. Koh, D. J. Miller, *Solid State Commun.* **1986**, *60*, 217.
[20] A. D. Lad, C. Rajesh, M. Khan, N. Ali, I. K. Gopalakrishnan, S. K. Kulshreshtha, S. Mahamuni, *J. Appl. Phys.* **2007**, *101*, 103 906.
[21] M. A. Malik, P. O'Brien, N. Revaprasadu, *J. Mater. Chem.* **2001**, *11*, 2382.
[22] T. A. Kennedy, E. R. Glaser, P. B. Klein, R. N. Bhargava, *Phys. Rev. B* **1995**, *52*, R14 356.
[23] a) R. E. Kremer, J. K. Furdyna, *Phys. Rev. B* **1985**, *31*, 1. b) H. A. Sayad, S. M. Bhagat, *Phys. Rev. B* **1985**, *31*, 591. c) S. B. Oseroff, *Phys. Rev. B* **1982**, *25*, 6584. d) S. B. Oseroff, R. Calvo, Z. Fisk, F. Acker, *Phys. Lett. A* **1980**, *80*, 311.
[24] A. Deneuville, D. Tanner, P. H. Holloway, *Phys. Rev. B* **1991**, *43*, 6544.
[25] A. K. Arora, E.-K. Suh, U. Debska, A. K. Ramdas, *Phys. Rev. B* **1988**, *37*, 2927.
[26] V. G. Pol, S. V. Pol, N. Perkas, A. Gedanken, *J. Phys. Chem. C* **2007**, *111*, 134.
[27] N. Shimodaira, A. Masui, *J. Appl. Phys.* **2002**, *92*, 902.
[28] V. Barbarossa, F. Galluzzi, R. Tomaciello, A. Zanobi, *Chem. Phys. Lett.* **1991**, *185*, 53.
[29] a) H. Waldmann, C. Benecke, W. Busse, H.-E. Gumlich, A. Krost, *Semicond. Sci. Technol.* **1989**, *4*, 71. b) D. F. Crabtree, *Phys. Status Solidi A* **1974**, *22*, 543.
[30] S. V. Pol, V. G. Pol, V. G. Kessler, G. A. Seisenbaeva, L. A. Solovyov, A. Gedanken, *Inorg. Chem.* **2005**, *44*, 9938.
[31] S. V. Pol, V. G. Pol, I. Felner, A. Gedanken, *Eur. J. Inorg. Chem.* **2007**, 9938.
[32] a) G. Milazzo, S. Caroli, V. K. Sharma, in *Tables of Standard Electrode Potentials*, Wiley, Chichester, UK **1978**. b) A. J. Bard, R. Parsons, J. Jordan, in *Standard Potentials in Aqueous Solutions*, Marcel Dekker, New York **1985**.
[33] V. G. Pol, S. V. Pol, A. Gedanken, V. G. Kessler, G. A. Seisenbaeva, M.-G. Sung, S. Asai, *J. Phys. Chem. B* **2005**, *109*, 6121.
[34] F. Martelli, M. Piccin, G. Bais, F. Jabeen, S. Ambrosini, S. Rubini, A. Franciosi, *Nanotechnology* **2007**, *18*, 125 603.
[35] V. Schmidt, U. Gosele, *Science* **2007**, *316*, 698.
[36] H. T. Lin, D. H. Rich, A. Konkar, P. Chen, A. Madhukar, *J. Appl. Phys.* **1997**, *81*, 3186.